

Visualisation of water droplets during the operation of PEM fuel cells

T. Ous*, C. Arcoumanis

Energy and the Environment Research Centre, School of Engineering & Mathematical Sciences, The City University, London, United Kingdom

Received 16 January 2007; received in revised form 13 March 2007; accepted 29 April 2007

Available online 5 May 2007

Abstract

A transparent proton exchange membrane fuel cell (PEMFC) has been designed to enable visualisation of water droplets during its operation. Images of the formation of droplets on the surface of the gas diffusion layer (GDL) on its cathode side, which result in water accumulation and blockage to the airflow channels, were recorded using a CCD camera. Measurement of the cell current and droplet characterisation have been carried out simultaneously and the effect of the airflow and external resistive load has been quantified. The droplet images show that water accumulation occurs first in the middle channels of a serpentine reactant-flow fuel cell design and that no droplets are formed at the bends of the flow channels. Water blockage to the airflow path was caused by the overlapping of two land-touching droplets developing on each side of the channel. Flooding was found to be more susceptible to the airflow than the other test operating conditions.

© 2007 Elsevier B.V. All rights reserved.

Keywords: PEMFC; Flooding; Water droplets; Gas diffusion layer (GDL); Airflow

1. Introduction

Successful water management in the proton exchange membrane fuel cell (PEMFC), particularly on its cathode side, is considered vital to achieving high performance and stability in the output power of the fuel cell [1–5]. Not enough water in the polymeric membrane layer results in reduction of the ionic conductivity of the cell [6,7], whereas too much water in the cell prevents further access of the reactant air and causes flooding in the reactant channels [8,9]. The water transport within the fuel cells was investigated numerically in previous studies [10–21]. A model for calculating the water balance in the membranes of polymer electrolyte fuel cells was presented in [10]; it estimates the total amount of water under various operating conditions. A similar investigation was carried out in [11] where the transient behaviour of the water transport in the membrane layer was analysed in order to identify effective control schemes for enhancing the performance of fuel cells. A detailed model of the single-phase flow through porous materials has been presented in [12,13]. A three-dimensional non-isothermal model [14] was used to compute the water flow as well as the heat management in a PEM fuel cell. This model determines the water transport in

the polymer membrane, the phase change of water in the cathode porous medium and the capillary flow in the gas channels. The influence of these processes on fuel cell performance has been numerically evaluated. In [15] a two-dimensional flow mixture model has been developed to simulate the water in the cathode of PEM fuel cells. In particular, the formation and distribution of the two-phase (air and water vapour) flow in the gas-diffusion layer and the reactants flow channel was predicted as a function of the current density, membrane properties and operating conditions. More advanced two-phase flow models were presented in [16–20]. A model for the transport of reactants and products in PEM fuel cells has been used in [17] to investigate the operating limits of PEM fuel cells using the unsaturated flow theory. In [18,19], a fully three-dimensional model simulating the species transport and the reactions in both the anode and the cathode flow channels, the catalyst layer and the proton exchange membrane (PEM) has been developed and presented. The multi-component mixture model of [16] was also used to simulate the transport of reactants and products in the air cathode of a PEM fuel cell. Water transport and distribution were classified by a threshold current density corresponding to the first appearance of liquid water at the membrane/cathode interface. The simulation results reveal that the capillary force is dominant for water transport inside the hydrophilic structure of the GDL. The investigations in [20] have focused on the behaviour of water in the air–water serpentine flow channels. Using the volume-of-fluid

* Corresponding author. Tel.: +44 20 7040 0113; fax: +44 20 7040 8101.
E-mail address: t.ous@city.ac.uk (T. Ous).

Nomenclature

f_{GDL}	water flow-rate through the GDL (L s^{-1})
GDL	gas diffusion layer
MEA	membrane electrode assembly
RH	relative humidity (%)
$w_{\text{air in}}$	water of the inlet airflow (L s^{-1})
$w_{\text{air out}}$	water of the outlet airflow (L s^{-1})
w_{prod}	water produced by fuel cell (L s^{-1})
w_{Surface}	water on the GDL surface (L s^{-1})

(VOF) model, it was shown that the bends of the serpentine flow channels have a significant effect on the flow field and that water flooding occurs in the ‘post bend’ section of a micro-channels cell design. This flooding was predicted to block the supply of reactants to the reaction sites and, in extreme cases, to block the reactant transport inside the flow channel, which reduces the performance of the fuel cell. The water distribution on the surface of the membrane was also predicted in [21] using a three-dimensional computational fluid dynamics (CFD) model, which showed that the local value of the water content increases from the inlet towards the outlet of the flow channels. On the other hand, the diagnostic tool applied in [22] was able to estimate the water distribution in a PEM fuel cell during operation. The membrane resistance and electron diffusivity (MRED) method was used to measure the resistance of the membrane, which relates to the water concentration in the cell and to reveal that more water accumulates in the middle flow channels.

The observed flooding in the airflow channels of the cell has been also investigated experimentally [5,8,9]. Measurement of the polarization curve was performed in [5] under various reactant humidity conditions and the results revealed that, during membrane dehydration, the fuel cell current density experiences rapid oscillations. In addition, membrane dehydration and water flooding cause reduction in the fuel cell performance. Visualisation of flooding was presented and discussed in [8,9]. In both experiments, the endplate on the cathode side was made of transparent material to enable optical access into the airflow channels so that water formation and flooding on the surface can be observed. The experimental set-up used in [9] allows simultaneous evaluation of the current, temperature and water distribution in a PEM fuel cell under operation. The visualisation results are in agreement with the conclusions drawn in [22] that water flooding occurs in the middle channels of the serpentine flow design. These results have also revealed that high air stoichiometry may prevent the occurrence of flooding which can raise the temperature and reduce the current density of fuel cells. Clear images of water accumulation inside the cathode flow channels were presented in [8]. The current density of the cell was measured as a function of the operating time while flooding was gradually developing in the channels. Useful to note that the observation in [8,9] was made when flooding had already occurred in the flow channels, but not during the droplets’ formation on the surface. Images of droplets on the surface of the GDL were obtained in [23] but for the rather limited case of the direct methanol fuel cell

(DMFC) type. In the present paper, images of droplet formation on the surface of the widely used proton exchange membrane fuel cell type are presented and discussed. This stage is considered quite critical since it takes place just before flooding. All images were processed simultaneously with the cell current. The characteristics of the first droplet to appear on the PEM’s surface have been compared under various airflow and external load conditions. Finally, droplet detachment from the surface by the increasing airflow stream has also been examined in order to quantify the droplet critical detachment values.

The production of water during the electrochemical reaction in a fuel cell takes place at the catalyst layer of the cathode. The amount of water produced is directly proportional to the molar mass of the reactants. The state of the water, which can be in either vapour or liquid form, is determined by the operating temperature of the cell. At the start of the reaction, most of the water travels towards the membrane layer. Once the membrane becomes saturated, the water starts to permeate through the gas diffusion layer (GDL) and later appears in the airflow channels as droplets. The flow of liquid and gas within the porous GDL is very difficult to estimate due to the complexity and the heterogeneity of the GDL structure. A number of models have been developed to simulate this flow. Richard’s model, for instance, examines a single-phase flow of water in the porous medium [24]; it is based on the assumption that the air present in the unsaturated zone has infinite mobility, i.e. it is at atmospheric pressure and moves without interfering with water and/or the contaminant. The Fractional flow model [25], on the other hand, includes the air as a separate phase following a two-phase flow approach, but it assumes that the viscosity of each phase is constant. However, under realistic fuel cell conditions, the intrinsic permeability and dynamic viscosity of both gas and water do not remain constant. The variation of these two values is attributed to the following factors: (a) the dynamic production of liquid water in the catalyst layer; (b) the change of the temperature distribution in the GDL particularly between local points; (c) the flow of electrons travelling along the GDL; and (d) the disordering in the carbon particles carried by the water flow which may slightly affect the fractional coefficient value and, hence, the permeability. The Dusty Gas model [26] is probably giving a more accurate estimate of the flow but requires many variables to be identified of which some can only be obtained experimentally. A more convenient method is to measure the amount of water in the airflow channels after the cell reaches a steady state. By measuring the water (i) produced at the catalyst, (ii) present on the surface of the channels, and (iii) contained in the inlet/outlet airflow stream, it is possible to quantify the water velocity across the GDL assuming that no water is able to travel towards the fully saturated membrane. Fig. 1 illustrates this approach more clearly.

2. Experimental system

2.1. Design of the transparent PEM fuel cell

In order to visualise the formation of water droplets in a PEM fuel cell, it is necessary to have optical access into the cathode

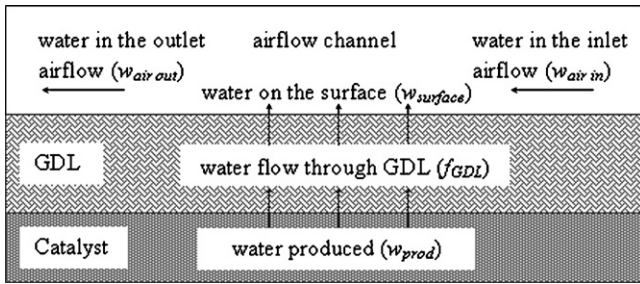


Fig. 1. Experimental approach for water flow rate estimation in the direction of the GDL surface.

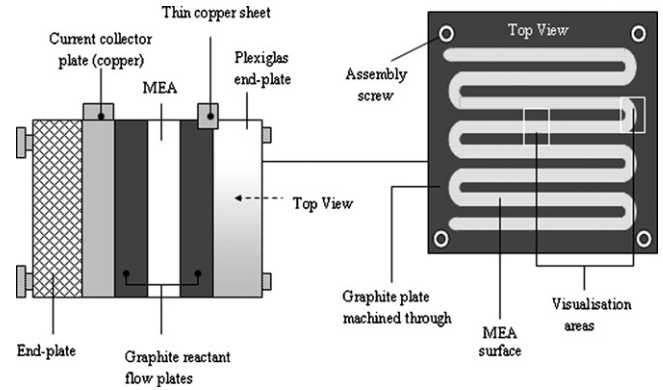


Fig. 2. Schematic diagram of the transparent PEMFC.

flow channels. Fig. 2 illustrates the design of the cell used in these tests. A transparent Plexiglass window was placed at the top of the graphite reactant-flow plate to allow droplet visualisation. A thin copper sheet was inserted in-between to collect the electric current produced by the cell. The flow channels of both the anode and cathode were machined in serpentine shapes with a channel width of 1.5 mm, a depth of 1.5 mm, and a length of 655 mm. The total number of channels in each plate was 13; they were equally spaced by lands, also called the ribs, of 1.5 mm width. The single cell uses a Johnson Matthey membrane-electrode-assembly (MEA No. 04-1879-03, Pt loading 3.5 mg m^{-3} , active area 25 cm^2) sandwiched between two Toray carbon papers (TGP-H-060). The complete unit was assembled using isolating screws located on the four corners, and a compressive torque of 12 Nm was applied across the unit.

2.2. Set-up

The experimental set-up is illustrated in Fig. 3. Hydrogen was supplied to the cell from a high purity (99.9%) dry hydrogen cylinder. The reactant air was humidified before entering the cell by a humidifier unit which consists of a series of atomisers (Norgren LO7-200-MPQG) capable of humidifying dry air from 30% RH to higher humidity values of 50–100% RH. The reactants air and hydrogen were regulated by the mass flow controllers CT Platon ($0.05\text{--}0.75 \text{ L m}^{-1}$) for hydrogen and JonCons ($0.2\text{--}5 \text{ L m}^{-1}$) for air. The pressure of the inlet/outlet reactant gases was measured in close proximity to the cell using

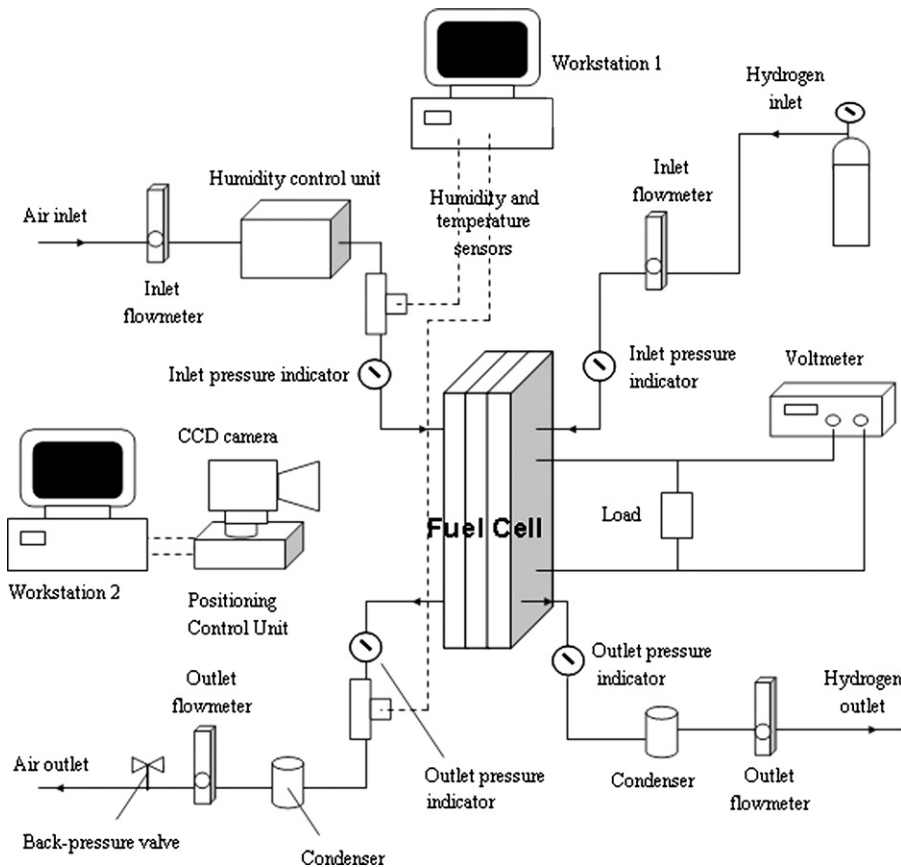


Fig. 3. Schematic diagram of the Experimental Set-up.

Table 1
Operating conditions of the performed experiments

Experiment no.	Inlet flow rate (mL m^{-1})		Air inlet humidity RH (%)	Reactants inlet pressure (psi)	External load (Ω)	Cell temperature ($^{\circ}\text{C}$)
	Air	H_2				
Exp. 1	12.1	25	20	Ambient	1.3	25
Exp. 2	4.86	25	75	Ambient	1.3	25
Exp. 3a	4.86	25	20	Ambient	1.3	25
Exp. 3b	12.1					
Exp. 3c	24.3					
Exp. 3d	219					
Exp. 4a	4.86	25	75	Ambient	1.3	25
Exp. 4b	12.1					
Exp. 4c	73					
Exp. 4d	219					
Exp. 5a	24	25	20	Ambient	0.6	25
Exp. 5b					1.2	
Exp. 5c					10	
Exp. 6	12.1	25	20	Ambient	0.6	25

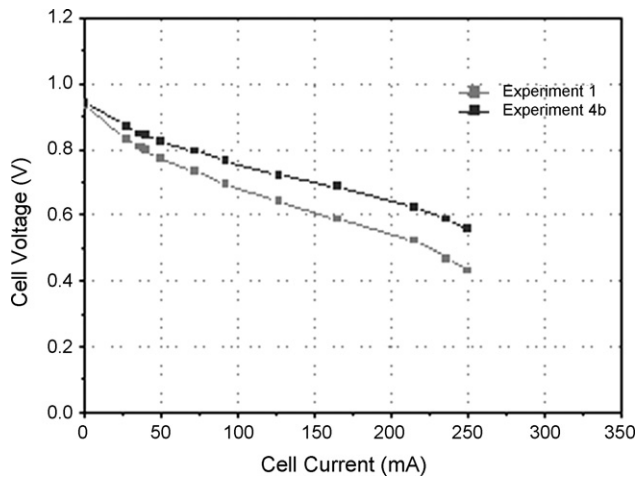


Fig. 4. Fuel cell polarization curve under the tested ambient operating conditions.

Stiko pressure indicators. At the output, a Clarke Air condenser was installed in order to collect the liquid water preventing the outlet flowmeters from fluctuating through flooding. The humidity and temperature of the air inlet and outlet was measured using built-in k-type sensors (Honeywell HIH-3610 and HEL-700 series). The data was transferred into Workstation 1 via a data acquisition system (National Instrument PCI-6225), and processed using the compatible Labview 7 software. The fuel cell current was measured using a Black Star 3225 multi-meter device. The external load used in these tests was simply a series of electric resistors, which were manually placed across the cell. A CCD digital camera (Sensi-Cam) was used to record all droplet images on the surface with a delay time of 100 ns to 10 ms; the obtained images were then processed in Workstation 2.

2.3. Operating conditions

Six experiments were carried out in this investigation. The operating conditions of these tests are listed in Table 1. The cell temperature maintained at ambient conditions (25°C), which

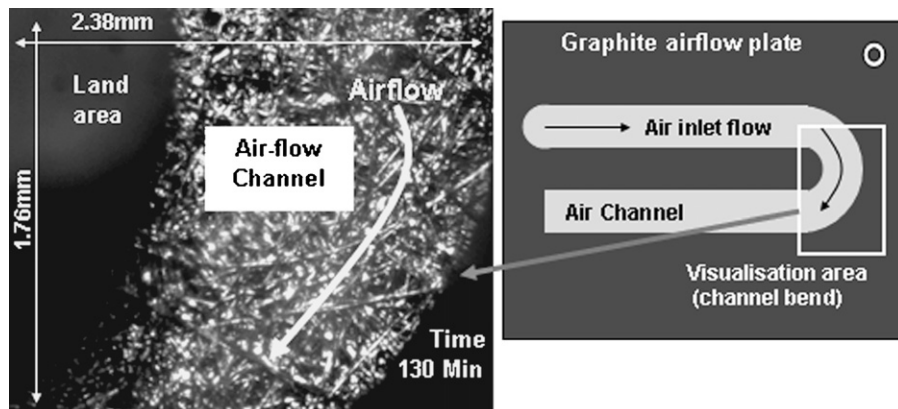


Fig. 5. Surface visualisation at the bend area of the flow channels (Experiment1).

represented the temperature of the cell during testing. Experiments 1 and 2 were performed to analyze droplet formation and flooding phenomena under dry (20% RH) and humidified (75% RH) air inlet conditions, respectively. Experiments 3–5 examined the effect of airflow and external load while Experiment 6 estimated the droplets critical detachment force from the surface. Between each of these experiments, dry air was blown inside the cell through the flow pipes for about 10 min to remove any water

left over and allow reproducible initial conditions to be obtained. The fuel cell was operated with dry hydrogen gas at a constant voltage of 520 mV using a fixed external load. Flow visualisation was focused at the bend and at the central location of the middle flow channels of the cell, as illustrated in Fig. 2. The presented droplet images and related conclusions have been confirmed by repeating the experiments a few times under identical operating conditions.

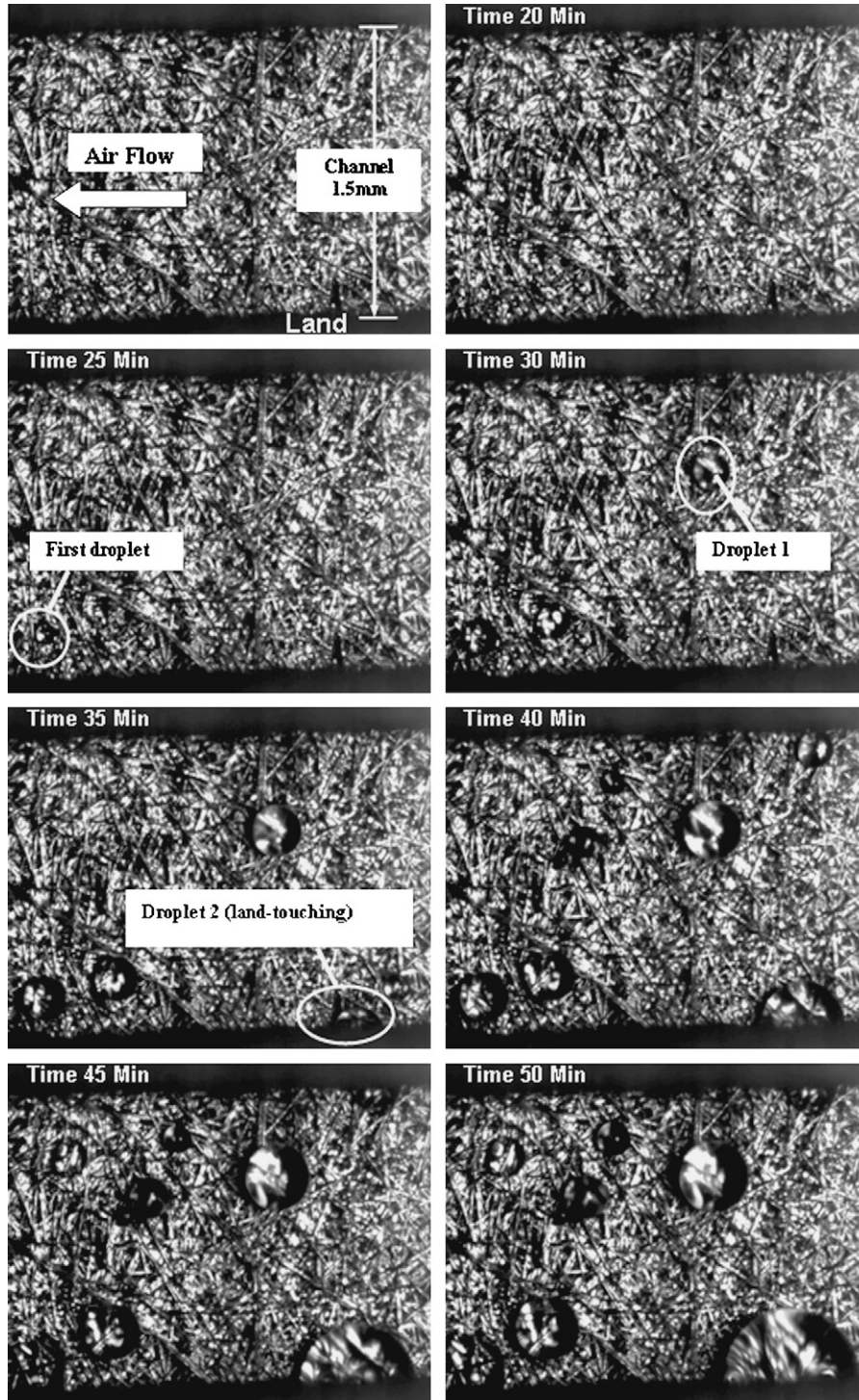


Fig. 6. Experiment 1: droplet formation during early fuel cell operation (0–50 min).

3. Results and discussion

3.1. Polarization curve

Fig. 4 shows a typical polarisation curve under the ambient operating conditions used in the tests described below. The performance of the cell was, unfortunately, lower than a typical operating fuel cell in order to allow improved droplet observa-

tion on the surface; this is due to the fact that lower current slows down the droplet formation rate.

3.2. Droplet formation on the surface

The images captured by the CCD camera show that liquid water starts to accumulate first in the middle flow channels. This means that flooding may happen first in that particular region

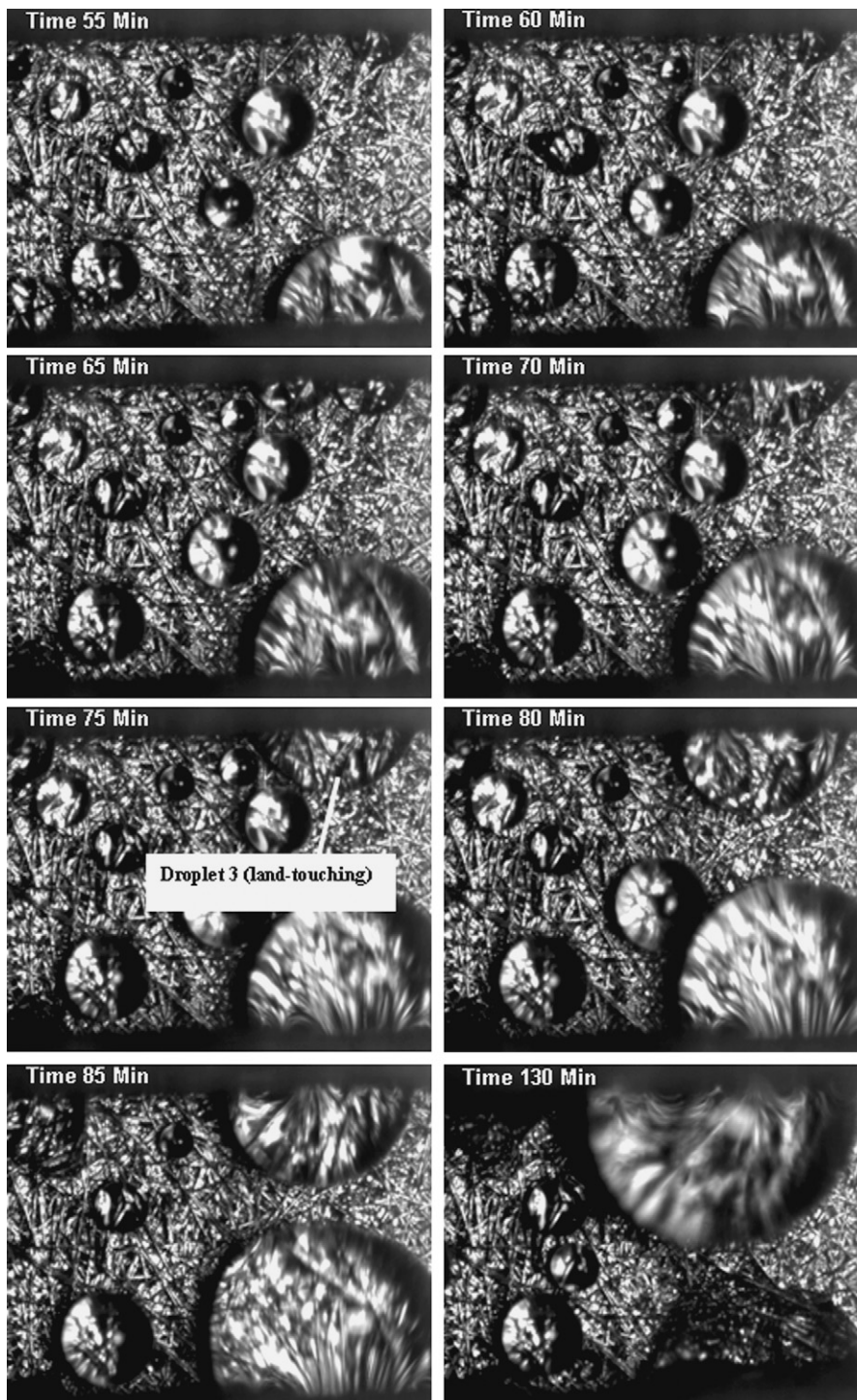


Fig. 7. Experiment 1: droplet formation during later fuel cell operation (55–130 min).

which can be attributed to the airflow in the channels. Since the air velocity in the middle channels is slower than at the inlets and outlet, the airflow is expected to be less capable of removing liquid water from the surface. The highest air velocities in the flow channels are at the bend areas. As shown in Fig. 5, no droplets were evident at the channel bends during the entire operational period (130 min).

Figs. 6 and 7 show a sequence of droplet images forming in the middle channels with an interval of 5 min between each frame. It can be observed from these images that the first droplet becomes visible after 25 min from the start of operation, which is the time required for water to permeate through the gas diffusion layer and to appear on the surface. At 30 min, two new droplets start growing while more new droplets appear on the surface. The droplet developed at the sidewall of the channel, land-touching (droplet 2), grows faster than those exhibiting no contact with the wall. This land-touching droplet 2 continues to grow until the 85th min where it coalesces with a neighbouring droplet (droplet 1) forming a new, larger droplet. Further water accumulation continues in the period between 85 and 130 min and, as a result, the flow channels become increasingly filled with water.

The water droplets appear on the surface in different sizes and nucleate at certain locations. The average diameter of droplets with no contact with the sidewall, the so-called non land-touching droplets, ranges from 0.1 to 0.6 mm. Their size is much larger than the size of the pores within the GDL due to the continuous feeding of water from the GDL and the coalescence of neighbouring droplets on the surface. It has been observed during testing that this increase in droplet size happens instantaneously rather than gradually. The diameter of droplet 1, shown in Fig. 6, increases from 0.2 to 0.26 mm in less than 0.1 s. But its size stays the same for the next 5 min until the droplet starts increasing again in a similar fashion.

The formation rate of droplet 1 has been estimated under the operating conditions of Experiment 1. The change of droplet's boundary, before the coalescence with a neighbouring droplet, is measured from the centre of the droplet. The results show that droplet 1 has grown by around 0.07 mm (23% of its size) in the period between 40 and 60 min, which gives an average formation rate of $3.5 \mu\text{m min}^{-1}$. A similar estimate for droplets 2 and 3 in Fig. 8, which were randomly selected, resulted in a formation rate of $8 \mu\text{m min}^{-1}$ and $2.6 \mu\text{m min}^{-1}$, respectively. The

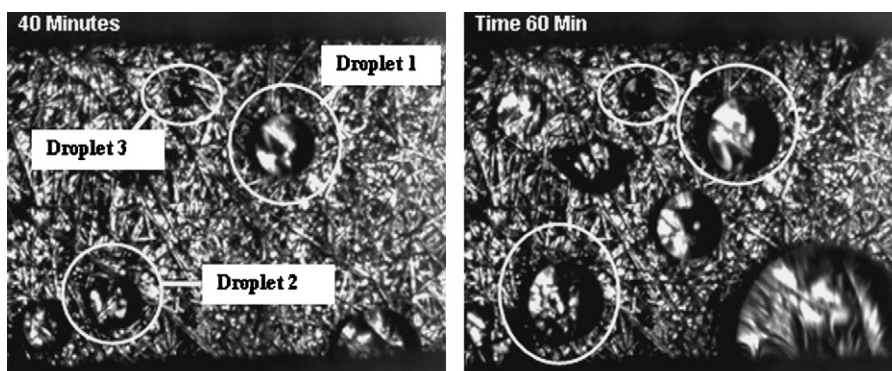


Fig. 8. Droplet formation between 40 and 60 min (Experiment 1).

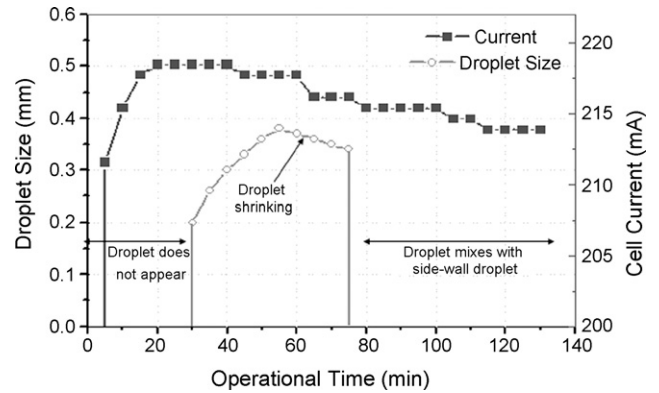


Fig. 9. Experiment 1: fuel cell current during droplet formation on the surface.

observed difference in the droplet formation rates is probably attributed to the heterogeneous internal structure of the GDL, which affects the surface tension distribution on the surface of the membrane.

Measurement of the cell current was made during the droplet formation process on the surface with an interval of 5 min. Fig. 9 shows the variation in cell current with respect to droplet size, for droplet 1 in Fig. 6, over the entire operational period (130 min). It can be seen from Fig. 9 that the cell produces a current of 218.5 mA before any droplet appears on the surface; droplet 1 appears with an initial diameter of 0.2 mm. The cell current at this instant stays at the same level of 218.5 mA and remains constant until the droplet reaches a size of 0.3 mm in 40 min. The current value then reduces slightly to 217.7 mA while the droplet is still growing to reach its maximum size of 0.38 mm. In the 60 min frame, the droplet starts to get smaller in size. The droplet at this instant has probably been pushed into the GDL by the airflow as a result of its increased cross-sectional area in the direction of the airflow. The shrinking process continues until the droplet combines in the 80 min frame with land-touching droplet 2. By the end of the testing after 130 min, more water accumulates in the channels causing the cell current to drop to 213.8 mA.

3.3. Complete flooding

The continuing accumulation of water results, at later stages, into complete occupation of the channel where water blocks

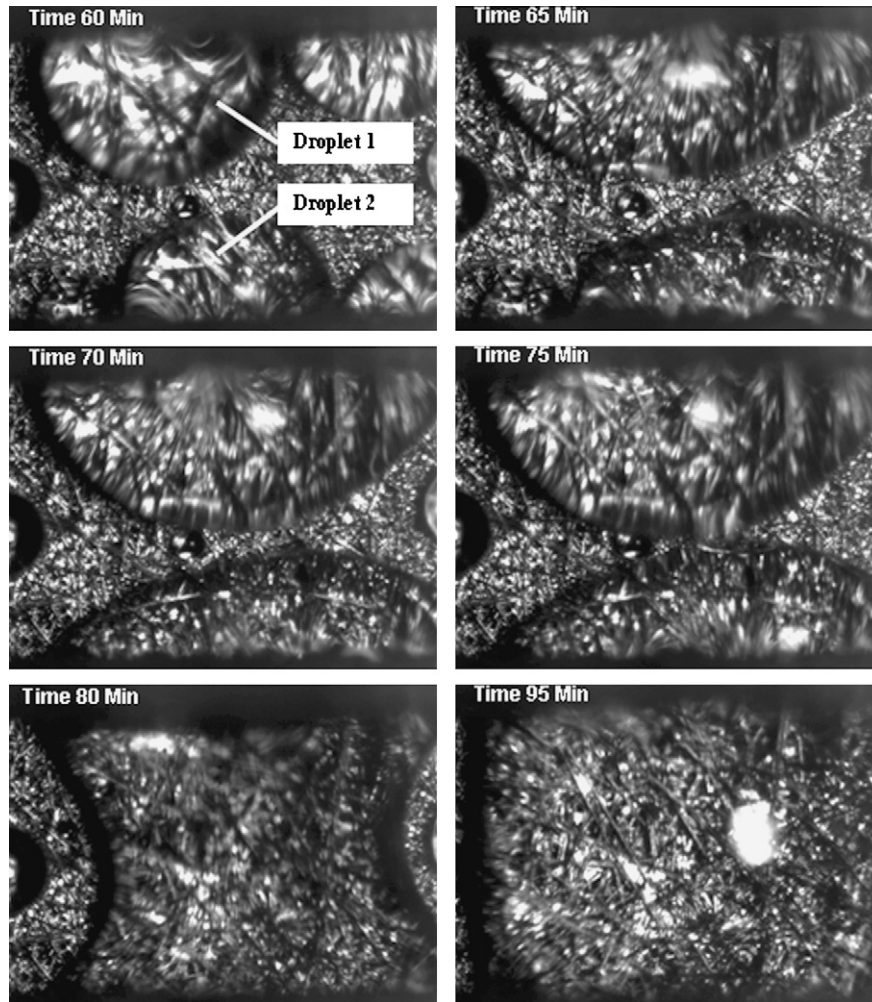


Fig. 10. Experiment 2: liquid blockage of the airflow channel.

the airflow. Fig. 10 shows the case where liquid water completely fills the area of visualisation of the channel. The two land-touching droplets in each side, droplet 1 and droplet 2, grow further during the period between 65 and 75 min, closing the gap between each other. In the 80-min frame, they combine forming a larger liquid volume with two concave edges, which soon expand along the channel.

3.4. Water accumulation at various operating conditions

The timing of appearance of the first droplet on the surface was compared for various airflow and external load conditions. The aim of this test was to identify the key parameters that influence most water accumulation in the channel. From these measurements, an effective technique to prevent flooding of channels could be developed. In Experiment 3, four different airflow scenarios have been examined under a constant load of 1.3Ω . Fig. 11 shows the time of droplet appearance on the surface versus inlet airflow rate for these four cases. It can be seen from the figure that the droplet appears on the surface 7 min earlier as the airflow increases from 4.86 to 24.3 mL m^{-1} . When the flow reaches 219 mL m^{-1} as in case d, no droplet was formed. It can

be argued that a higher airflow delays the formation of droplets on the surface as it carries away more water. However, the more air enters the cell, the more the mass of reactant air that is available to participate in the electrochemical reaction of the cell and, hence, the greater the production of water and current. The fact is

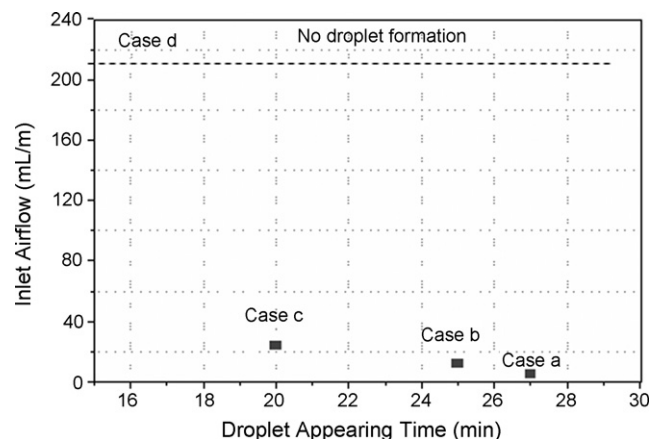


Fig. 11. Droplet appearing time on the surface at different dry airflow rates (Experiment 3).

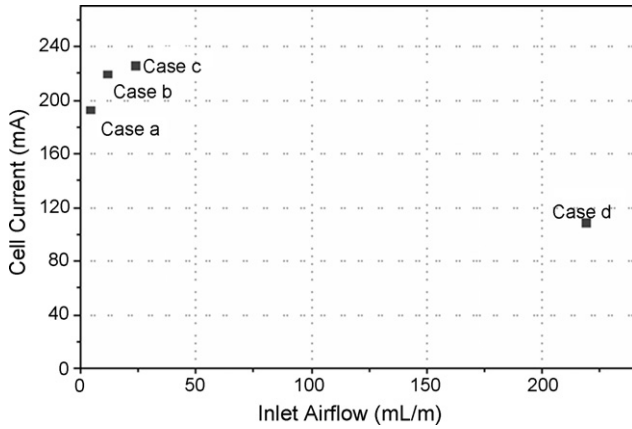


Fig. 12. Effect of dry airflow rate on fuel cell current (Experiment 3).

that this holds true only for low and intermediate airflow rates. Once the airflow reaches a certain dehydration value, the air dries out the surface completely. This can be clearly seen from the value of the cell current at 219 mL m^{-1} airflow. As shown in Fig. 12, the current seems to be proportional to the inlet airflow. However, when the flow reaches 219 mL m^{-1} , there is a significant decline in current to 109 mA. It is expected that the high airflow caused a partial dehydration to the membrane, which leads to reduced conductivity and, hence, lower cell current.

Experiment 4 examines the effect of airflow but this time, under humidified inlet airflow conditions. The results of this test are presented in Figs. 13 and 14. The droplet at the lower operating airflow appears earlier than at the high airflow conditions. Droplets were observed 19 min later when the airflow increased from 4.86 to 73 mL m^{-1} . The difference in these results from those of Fig. 11 is due to the humidity of the air, which accelerates water accumulation on the surface, making it harder for the low airflow to remove the water there. Again droplets were not observed on the surface at the higher airflow of 219 mL m^{-1} . This result implies, together with those of Fig. 11, that at high airflow conditions inlet air humidity has no significant effect on the water formation at the surface and that high flow rates are capable in preventing the occurrence of flooding.

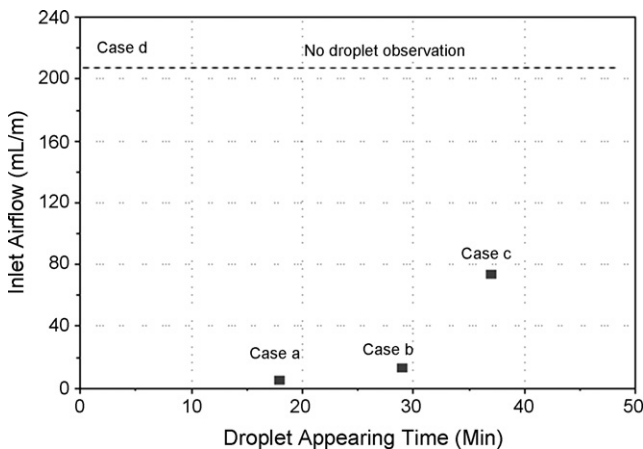


Fig. 13. Droplet appearing time on the surface at different humidified airflow rates (Experiment 4).

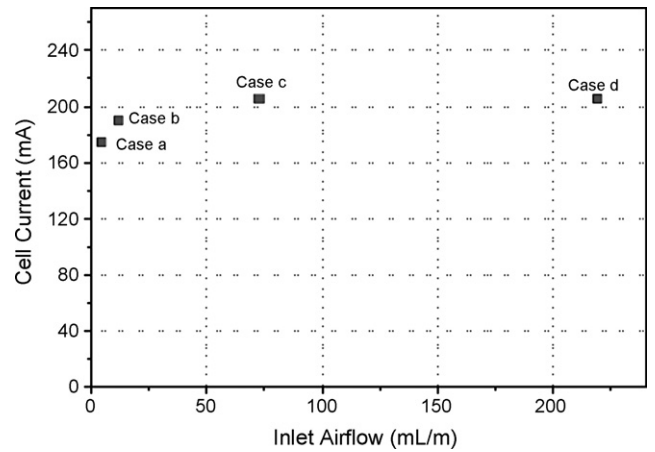


Fig. 14. Effect of humidified airflow rate on fuel cell current (Experiment 4).

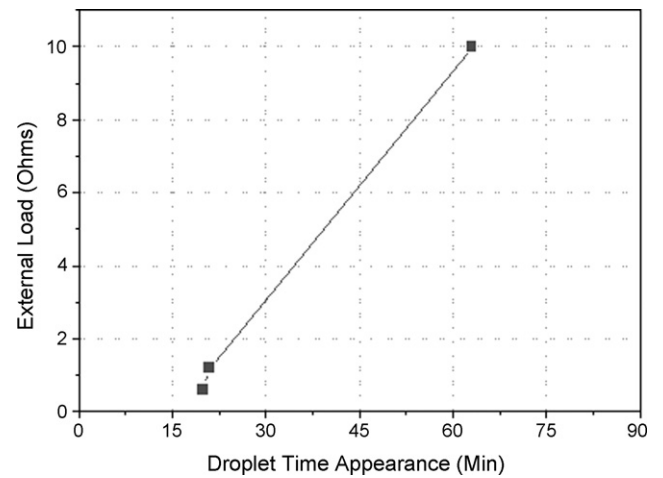


Fig. 15. Effect of the external load on droplet appearing time on the surface (Experiment 5).

Another difference between the results of Experiments 3 and 4 was identified. Fig. 14 shows that at the higher airflow rate of 219 mL m^{-1} , the cell current stays at the same value of 205 mA which implies that the amount of water in the inlet air

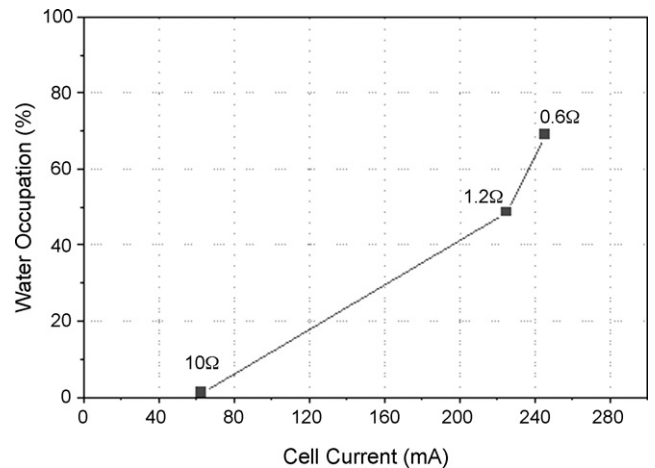


Fig. 16. Water occupation in the observed channel area vs. cell current after 80 min of operation (Experiment 5).

stream was probably enough to maintain the fuel cell membrane hydrated.

Experiment 5 examines the effect of the external load on the droplet appearance time on the surface. Three different loads (0.6–1.2–10 Ω) were used in these tests and the results are shown in Fig. 15. It can be clearly seen that higher loads delay the droplet formation on the surface. The droplet formed when using a 10 Ω load was observed 43 min later than for the 0.6 Ω load.

This result was expected since more current is produced from a small external load. The percentage of water occupying the observation area of the channels after 80 min of operation is shown in Fig. 16 under the three load conditions. Water production seems to be proportional to the cell current. However, the gradient becomes smaller at high current values. This change in gradient implies that water has filled some of the pores within the GDL, thus limiting the access of the reactant air. According

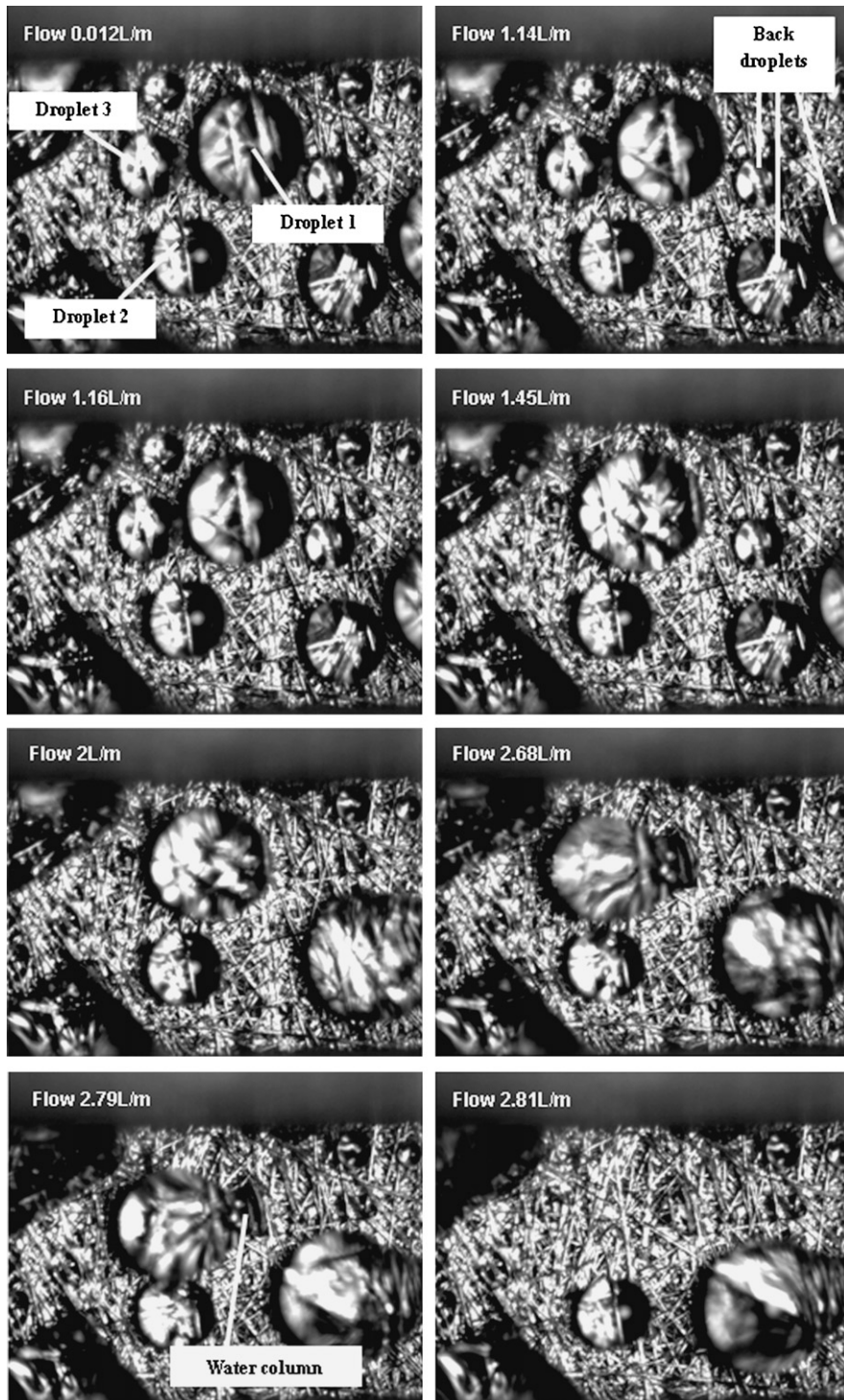


Fig. 17. Droplet behaviour on the surface at different airflow rates (Experiment 6).

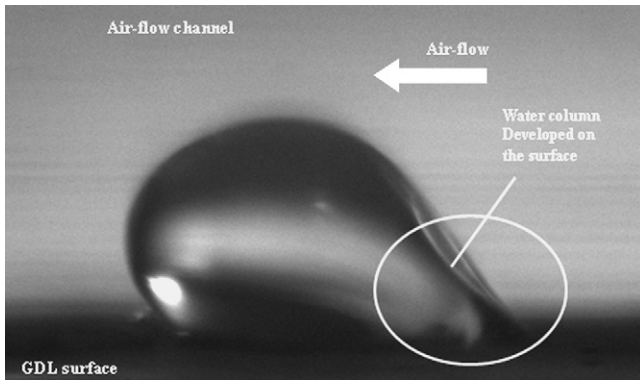


Fig. 18. Image of droplet detachment from the GDL surface by the airflow [27].

to Fig. 16, the percentage of water in the observation channel has increased by 57 times as the load reduces from 10 to 0.6 Ω .

3.5. Droplet detachment

Droplet detachment from the surface of the GDL by the incoming airflow stream has not been observed during the operation of the fuel cell under the examined operating conditions. The operating airflow was either too high preventing the formation of droplets or not high enough to detach them once formed. The only way for detachment to take place is to let the droplets grow on the surface first and then gradually increase the airflow until they are completely detached. The images in Fig. 17 show the behaviour of the droplets on the surface against the applied airflow; droplet 1 (0.61 mm) and droplet 2 (0.42 mm) have not been affected by an airflow of 1.14 L m^{-1} . At the higher flow rate of 1.16 L m^{-1} , droplet 1 starts to wobble while droplet 2 is still resistant to the flow. Droplet 1 combines with droplet 3 at 1.45 L m^{-1} due to its wobbling in the direction of the airflow. The shape of droplet 1 at that moment is slightly deformed. The effect of the flow on droplet 2 starts at 1.71 L m^{-1} . The wobbling of droplet 1 continues while the flow gradually increases. The three droplets within the visualisation window collide with each other at the 2 L m^{-1} flow rate. Droplet 1 becomes more deformed at 2.57 L m^{-1} but at 2.68 L m^{-1} it struggles to main-

tain its contact with the surface whereas droplet 2 continues to wobble. At 2.79 L m^{-1} , an interesting case was observed where a liquid column was developed keeping droplet 1 attached to the surface. This phenomenon displays the final shape for the droplet before total detachment from the surface, as observed in Fig. 18 [27]. Finally at 2.81 L m^{-1} , droplet 1 detaches completely from the surface.

Fig. 19 shows the air velocity which cause different droplet sizes to detach from the GDL surface. The results confirm that smaller droplets have higher resistance and/or exhibit higher surface tension, thus maintaining better contact with the surface than larger droplets.

4. Conclusions

A transparent proton exchange membrane fuel cell was used to visualise the water droplet formation during its operation. Images of droplets developing on the surface of the gas diffusion layer were recorded which show that water accumulates first in the middle flow channels and that no accumulation takes place at the bend areas. Two types of droplet have been identified during visualisation: land-touching and non land-touching droplets; the former appear to be larger in size and to grow relatively faster than the latter. The growth in size of the land-touching droplets was gradual whereas for the non-touching droplets it was instantaneous. The formation rate of these droplets was measured and found to be different depending on their location in the channel. It has also been observed that the overlapping between two land-touching droplets, on each side of the channel, can cause complete blockage to the airflow. Measurement of the fuel cell current during water production showed that the current gradually declines as more water fills the channels but this has no effect on the droplet formation on the surface. The shrinking of the droplet seems to be due to its increased cross-sectional area in the direction of the airflow, which may push the droplet back into the GDL.

Droplet formation on the surface has been examined under various operating conditions. The results show that, under dry air conditions, droplets start forming earlier in the case of a higher airflow. This increase in the molar mass of reactant air improves the electrochemical reaction of the cell and produces more water. The results, however, were different when humid air was used. This time the droplets appear first on the surface at a lower airflow rate. The accumulated water on the surface, as accelerated by the humid air, is hardly removed by the lower airflow rate. However, operating at a very high airflow rate under any of these conditions prevents droplet formation on the surface. The fuel cell current becomes more susceptible to the higher flow rate if the reactant air is dry. The measurements show a substantial decrease in the current value once the fuel cell operates under high airflow rate and dry air conditions. This drop is the result of partial dehydration of the membrane, which reduces its ionic conductivity.

The effect of external load on droplet formation at the surface was quite prominent. Droplets were observed on the surface later when the load across the cell was increased. Droplet detachment from the surface through increased airflow was investigated for

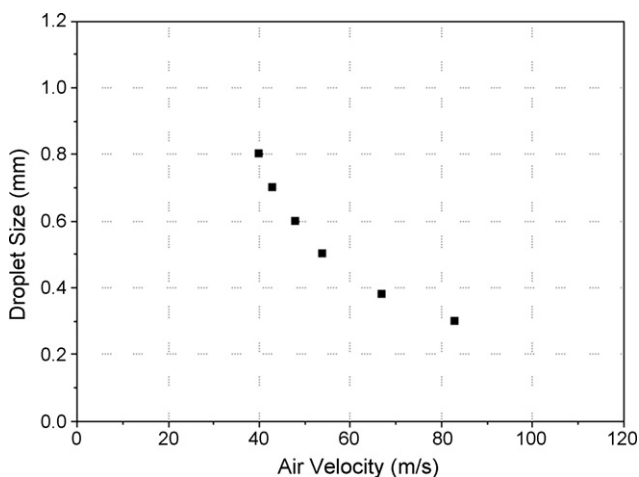


Fig. 19. Air velocity detachment for different droplet sizes (Experiment 6).

different droplet sizes. The results confirm that smaller droplets maintain better their contact with the surface than larger droplets, exhibiting higher adhesion force with the surface. The air velocity, which causes droplets to detach from the surface is inversely proportional to droplet size.

Acknowledgements

The authors would like to acknowledge the contributions to this programme of Dr. J.M. Nouri, Dr. M. Gavaises, Mr. Tom Fleming and Mr. Jim Ford.

References

- [1] T.V. Nguyen, M.W. Knobbe, *J. Power Sources* 114 (2003) 70–79.
- [2] Z. Qi, A. Kaufman, *J. Power Sources* 109 (2002) 469–476.
- [3] L.B. Wang, N.I. Wakayama, T. Okada, *Electrochem. Commun.* 4 (2002) 584–588.
- [4] D.L. Wood III, J.S. Yi, T.V. Nguyen, *Electrochim. Acta* 43 (1998) 3795–3809.
- [5] W.K. Lee, J.W. Van Zee, S. Shimpalee, S. Dutta, Presented at the 1999 International Mechanical Engineering Congress & Exposition, Nashville, 1999.
- [6] J.-C. Lin, H.R. Kunz, J.M. Fenton, in: W. Vielstich, A. Lamm, H.A. Gasteiger (Eds.), *Handbook of Fuel Cells: Fundamentals, Technology and Applications*, John Wiley & Sons, 2003, pp. 456–463.
- [7] R.F. Silva, M. De Francesco, A. Pozio, *J. Power Sources* 134 (2004) 18–26.
- [8] K. Tüber, D. Pócza, C. Hebling, *J. Power Sources* 124 (2003) 403–414.
- [9] A. Hakenjos, H. Muentzer, U. Wittstadt, C. Hebling, *J. Power Sources* 131 (2004) 213–216.
- [10] T. Okada, G. Xie, M. Meeg, *Electrochim. Acta* 43 (1998) 2141–2155.
- [11] F. Chen, H.-S. Chu, C.-Y. Soong, W.-M. Yan, *J. Power Sources* 140 (2005) 243–249.
- [12] A.G. Yiotis, A.K. Stubos, A.G. Boudouvis, Y.C. Yortsos, *Adv. Water Resour.* 24 (2001) 439–460.
- [13] K. Boomsma, D. Poulidakos, *J. Fluids Eng.* 124 (2002) 263–272.
- [14] L. Matamoros, D. Bruggemann, *J. Power Sources* 161 (2006) 203–213.
- [15] L. You, H. Liu, *Int. J. Heat Mass Transfer* 45 (2002) 2277–2287.
- [16] Z.H. Wang, C.Y. Wang, K.S. Chen, *J. Power Sources* 94 (2001) 40–50.
- [17] U. Pasaogullari, C.-Y. Wang, *Electrochim. Acta* 49 (2004) 4359–4369.
- [18] M. Hu, A. Gu, M. Wang, X. Zhu, *Energy Convers. Manage.* 45 (2004) 1861–1882.
- [19] S. Um, C.Y. Wang, *J. Power Sources* 125 (2004) 40–51.
- [20] P. Quan, B. Zhou, A. Sobiesiak, Z. Liu, *J. Power Sources* 152 (2005) 131–145.
- [21] S. Shimpalee, S. Greenway, D. Spuckler, J.W. Van Zee, *J. Power Sources* 135 (2004) 79–87.
- [22] J. Stumper, M. Lohr, S. Hamada, *J. Power Sources* 143 (2005) 150–157.
- [23] G.Q. Lu, C.Y. Wang, *J. Power Sources* 134 (2004) 33–40.
- [24] L.A. Richards, *Physics* 1 (1931) 318–333.
- [25] H.A. Kundsén, E. Aker, A. Hansen, *Transport Porous Media* 47 (2002) 99–121.
- [26] E.A. Mason, A.P. Malinauskas, *Gas Transport in Porous Media: The Dusty-Gas Model*, Elsevier Science Ltd., 1983.
- [27] A. Theodorakakos, T. Ous, M. Gavaises, J.M. Nouri, N. Nikolopoulos, H. Yanagihara, *J. Colloid Interface Sci.* 300 (2006) 673–687.